Computation of Unsteady Viscous Marine-Propulsor Blade Flows—Part 1: Validation and Analysis

E. G. Paterson
Hunter Rouse Graduate Fellow,
Currently, Assistant Research Scientist.
Assoc. Mem. ASME

F. Stern
Professor. Mem. ASME

Iowa Institute of Hydraulic Research and
Department of Mechanical Engineering,
The University of Iowa, Iowa City, IA
52242-1585

In this two-part paper, time-accurate solutions of the Reynolds-averaged Navier-Stokes equations are presented, which address through model problems, the response of turbulent propeller-blade boundary layers, and wakes to external-flow traveling waves. In Part 1, the Massachusetts Institute of Technology flapping-foil experiment is simulated and the results validated through comparisons with data. The physics of unsteady blade flows are shown to be complex with analogy to Stokes layers and are explicated through visualization and Fourier analysis. It is shown that convection induced steady/unsteady interaction causes deformation of the external-flow waves and is responsible for the upstream- and downstream-traveling pressure-gradient waves over the foil and in the wake, respectively. The nature of the unsteady displacement thickness suggests viscous-inviscid interaction as the mechanism for the response. In Part 2, a parametric study is undertaken to quantify the effects of frequency, foil geometry, and waveform.

Introduction

In comparison to other rotating machinery, marine propulsors are unique in that they are susceptible to cavitation and, more importantly for the work herein, operate in the thick hull boundary layer and/or appendage wakes. This creates a flow which, at design conditions, is inherently interactive and unsteady. Moreover, at off-design conditions (e.g., maneuvering) complex natural (i.e., vortex shedding from the hull) and forced (i.e., propulsor) unsteady interactions occur. Computational fluid dynamics (CFD) methods have been applied extensively to the steady-flow approximation of propeller/hull interaction. These methods typically use an interactive approach, i.e., a body-force propeller representation in a Reynolds-averaged Navier-Stokes (RANS) method obtained interactively using a vortex-lattice propeller-performance method for specified inflow (e.g., Stern et al., 1994a). CFD methods have also been applied to the steady-flow problem of open-water (i.e., uniform inflow) propeller-blade and wake flows both for idealized (Kim and Stern, 1990) and practical turboprop and marine propulsors (Stern et al., 1994b). Despite the advances made by these methods, the unsteady complete-configuration flow, whose understanding is critical for issues such as cavitation, vibration, and acoustics, remains as a computational Grand Challenge and requires both further CFD development and experimental fluid dynamics (EFD) validation data. Recent efforts, including those reported here, have been directed toward meeting this challenge by addressing issues of time-accurate RANS for fixed- and moving-boundary problems (Paterson, 1994), practical marine propulsors with simplified periodic inflows (Chen et al., 1994), and self-propelled maneuvering underwater vehicles (McDonald and Whitfield, 1996).

Historically, the rational approach for analysis of unsteady propulsor hydrodynamics has been through the use of two-dimensional models of propeller blade and wake flow, i.e., a foil embedded in vertical and horizontal traveling waves (gusts) at the dominant frequencies (i.e., up to reduced frequency of 10) of the ships nominal wake. As such, the model problem is directly related to the classical and fundamental work on unsteady boundary layers and unsteady lifting flows. However, both bodies of work have been approached with differing perspectives, i.e., as viscous- and inviscid-flow problems, respectively, thus creating a need for more comprehensive study. Nevertheless, the previous work provides a framework for understanding unsteady, viscous, lifting blade flows.

Nearly all work on unsteady boundary layers is for a flat plate subject to a uniform stream with superimposed temporal, spatial, or traveling horizontal-wave outer-flow oscillation. Most information, however, is for laminar and turbulent boundary layers with temporal-wave outer flow (e.g., Telionis, 1981; Spalart and Baldwin, 1989; Shima, 1993) where it is known that the response is characterized by small-amplitude Stokes-layer overshoots, phase leads, and streaming and, in addition, limited interaction between mean and turbulent motions. Spatial-wave outer flows, on the other hand, which are related to ship hydrodynamics problems involving free-surface piercing bodies with gravity waves, have only recently been put in context of Stokes layers (Choi et al., 1996). Choi et al. (1996) showed that Stokes-layer behavior is observed, but is significantly larger in amplitude than the temporal wave, and that nonlinear interaction between the zeroth- and first-harmonic velocity components result in an asymmetric wake response. Of most interest for the work here is the traveling-wave outer flow. However, as in the case of spatial waves, very limited information is available (Choi et al., 1996; Patel 1975, 1977). Choi et al. (1996) did show that for laminar flow, the boundary layer response to traveling waves was extreme, i.e., very large overshoots and large phase lags, for certain combinations of wave speeds and frequencies. Unfortunately, virtually no work exists for turbulent boundary layers subject to traveling waves, particularly at the level of resolution required to validate RANS methods and turbulence models and explicate the interaction between mean and turbulent motions.

The situation for unsteady lifting flows is similarly incomplete: the results are limited in range, most notably frequency, and contradictory since they resolve differing levels of physics.

Contributed by the Fluids Engineering Division for publication in the JOURNAL OF FLUIDS ENGINEERING. Manuscript received by the Fluids Engineering Division July 20, 1995; revised manuscript received September 23, 1996. Associate Technical Editor: G. Em Karniadakis.

For example, the pioneering linear potential flow theories for foils embedded in traveling vertical waves (Sears, 1941) and traveling waves with both vertical and horizontal components (Horlock, 1968) neglect interaction of the outer unsteady flow with the mean flow field and suffer frequency restrictions due to use of the steady Kutta condition. Nonlinear potential flow methods (Goldstein and Atassi, 1976) show that steady/unsteady interaction significantly accelerates and distorts the waves resulting in a much different lift response. As further shown by Basu and Hancock (1978), this interaction additionally creates a complex unsteady foil wake which is a combination of its shed vorticity due to lift and the deformed gust. Use of the steady Kutta condition in potential flow theories has been shown to be invalid (Poling and Telionis, 1986) for reduced frequencies $k = \omega L/2U_0$ above 2 due to nonzero loading at the trailing edge. More importantly, Poling and Telionis (1986) postulated, through visualization of strong curvature of the near-wake streamlines, that viscous-inviscid interaction may be an important feature of high-frequency gust flows. Finally, the wave characteristics of the pressure field, which are particularly important for acoustics and cavitation, differ significantly between theory and EFD and CFD. While the classical theories predict constant phase angle along the foil (i.e., a temporal-wave response), EFD (e.g., Commerford and Carta, 1974) and compressible Euler-equation CFD (Atassi et al., 1993; Adamcyzk and Brand, 1972) show upstream- and downstream-traveling pressure waves. No definitive explanation for this response has been advanced since most studies are either focused on other aspects (e.g., acoustic energy as opposed to purely hydro or aerodynamic sources) or limited in scope and/or range of parameters.

Obviously, there are many issues to be addressed and much work is required in understanding their relative importance, parametric dependencies, and relationship to practical applications. Therefore, the objectives of the present work are twofold. First, in Part 1, unsteady-flow calculations and validation through comparisons with the Massachusetts Institute of Technology (MIT) Marine Hydrodynamics Laboratory flapping-foil experiment (FFX) are presented. The results are discussed for steady and unsteady flow, including comparisons with the data, and an analysis provided to explicate the observed response. Second, in Part 2, a parametric study of frequency, waveform, and foil geometry is presented to relate the observations made in Part 1 to the classical and fundamental work, to further explicate the response, and to determine implications with regard to practical applications.

MIT Flapping-Foil Experiment

The FFX consists of a foil embedded in traveling vertical and horizontal waves generated by upstream pitching foils (Fig. 1) and was designed to provide detailed measurements for validation of unsteady CFD methods and determination of appropriate Kutta conditions for unsteady potential-flow methods. Details of the experimental objectives, apparatus, procedures, and uncertainty are documented by Rice (1991), Delpero (1992), and Horwich-Lurie (1993). Associated with FFX was the 29–30 March 1993 Office of Naval Research (ONR)/MIT Unsteady-Flow Workshop in which various groups of researchers submitted blind computations (i.e., with only the experimental conditions and boundary data) and met at the workshop for the comparisons with the data and discussion. Paterson and Stern (1993) provide a discussion of the Workshop results.

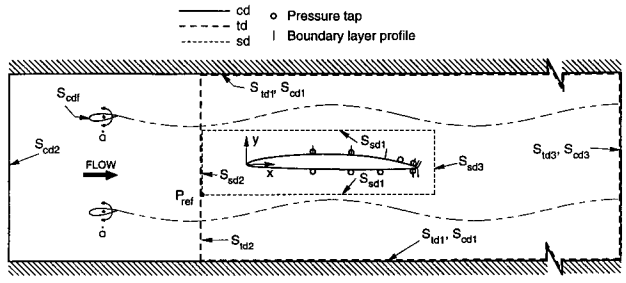

Fig. 1 Flapping-foil experiment geometry and solution domain boundaries

The experiments were performed in the closed-loop MIT Variable-Pressure Water Tunnel which has a 53 in long and 20 inches square test section and a freestream turbulence level of about 1 percent. The foil is a modified NACA 66 fixed at an angle of attack of 1.18–1.34 deg with transition set at $x = 0.105$ on both sides. Modifications were made to the foil geometry to account for blockage such that the foil in the tunnel produced the same steady pressure distribution as the unmodified foil in open-water conditions. The flappers are NACA 0025 and are driven by a variable-speed motor with an amplitude of 6 deg and a frequency of 16 Hz. The corresponding Re based on the foil chord length is 3.78×10^6 and the frequency parameter is $\xi = 3.6$.

Velocity and surface-pressure measurements were made using a two-component laser Doppler velocimeter and miniature pressure transducers, respectively. For the unsteady measurements, the value at each time step is the ensemble, or phase, average over 250 periods and had a temporal discretization of 180 points over the period.

Prior to the workshop, steady and unsteady (U, V) data was provided on the small domain boundaries and 60 percent of the tunnel domain inlet along with steady boundary-layer profiles. After the workshop, unsteady boundary-layer profiles and pressure data was provided at the locations shown in Fig. 1. In general, comparisons are made to the data whenever possible.

Computational Method

In the following, the method is briefly described, an overview is given of the solution domains, boundary conditions, and grid generation, and numerical uncertainty is discussed.

Description. The Reynolds-averaged Navier-Stokes (RANS) equations are written in the physical domain using Cartesian coordinates with x positive downstream, y normal to x, and the origin at the foil leading edge (Fig. 1) and are partially transformed (i.e., coordinates only) into nonorthogonal curvilinear coordinates such that the computational domain forms a simple rectangular parallelepiped with equal grid spacing. The transformed equations are reduced to algebraic form using finite-analytic (FA) spatial discretization (Chen and Chen, 1984), where the FA coefficients are obtained from a local analytical solution to the linearized momentum equations, and second-order accurate backward finite-difference temporal discretization. This results in a computational stencil that includes all eight neighboring nodal values and the values at the two previous time-steps. The overall solution procedure is based upon the two-step pressure-implicit split-operator (PISO) algorithm (ISSA, 1985) and a pressure equation derived from the discrete continuity equation. In step 1 of the algorithm, the implicit momentum equations are solved iteratively using line-ADI with under-relaxation and the pressure from the previous time step. Step 2 consists of iterations between line-ADI solution of the implicit pressure equation and an explicit velocity correction. In both steps of the algorithm, iterative convergence is required to ensure time accuracy and is measured using residuals based upon the difference between iterates. Also, the FA coefficients, which are dependent upon the local velocity, are updated at each step thus retaining the nonlinearity of the equations. Closure is attained through a quasi-steady application of the Baldwin-Lomax turbulence model with modifications to account both for the effects of wake asymmetry (Rodi and

Srinivas, 1989) and axial pressure gradients (Granville, 1987). Note that complete details of the methods used are presented in Paterson (1994).

Solution Domains and Boundary Conditions. The FFX was conducted such that calculations could be performed for a small domain with given boundary data, for a tunnel domain with a specified inflow, or for the complete domain, including the upstream flappers. At the workshop, the authors submitted blind computations using the small domain. Subsequent calculations included all three domains, including a complete-domain calculation using unsteady Chimera domain decomposition. All three domains (small, tunnel, and complete) are shown in Fig. 1. Referring to the notation in Fig. 1, the boundary conditions for the small domain are:

(1) On the top and bottom (S_{sd1}), U is from data, V is from continuity, and p is from an integrated form of the Euler equation.
(2) On the inlet (S_{sd2}), U, V are from data and p is from the axial Euler equation.
(3) On the exit (S_{sd3}), zero-diffusion and zero-pressure-gradient conditions are applied.

For the tunnel domain:

(1) On the tunnel walls (S_{td1}), slip boundary conditions are used, that is, $\partial U/\partial y = 0$, $V = 0$, and $\nabla p \cdot \mathbf{n} = 0$.
(2) On the inlet (S_{td2}), U, V is from a combination of data and an inviscid model and p is from the axial Euler equation.
(3) On the exit (S_{td3}), zero-diffusion and zero-pressure-gradient conditions are applied.

For the complete domain, the boundary conditions are the same as the tunnel domain except for:

1) On the inlet (S_{cd2}), uniform flow and zero-pressure-gradient conditions are used.
2) On the flapping-foils (S_{cdf}), the no-slip condition is used, that is, $U = -\alpha\xi \cos(\xi\tau)(y - y_r)$, $V = -\alpha\xi \cos(\xi\tau)(x - x_r)$, and $\nabla p \cdot \mathbf{n} = 0$ where α is the flapper amplitude, (x_r, y_r) is the center of rotation, τ is the nondimensional time, and ξ $(=\omega L/U)$ is the frequency parameter.

Grid Generation. Two grid-generation techniques were used depending on the domain and grid topology. EAGLE (Thompson, 1987) was used to generate C-grids for the foil in the small domain and the flappers in the complete domain. Algebraic H-grids were generated for both the tunnel and complete domains with hyperbolic tangent stretching functions and transfinite interpolation such that the grid spacing was controlled along the foil surface, leading and trailing edges, and the flapper wakes. For the complete domain, Chimera domain decomposition (Suhs and Tramel, 1991) was used to resolve the oscillating flappers by decomposing the domain into three separate, but coupled domains.

Numerical Uncertainty. The recent publication of ASME Standards and Guidelines for numerical uncertainty (Freitas, 1993) are important in signaling a new era in CFD development and application. Recently, Stern et al. (1996) critically reviewed the standards and guidelines, grouped them into documentation

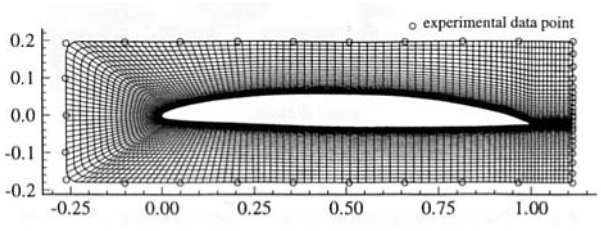

Fig. 2 Small-domain grid with data locations

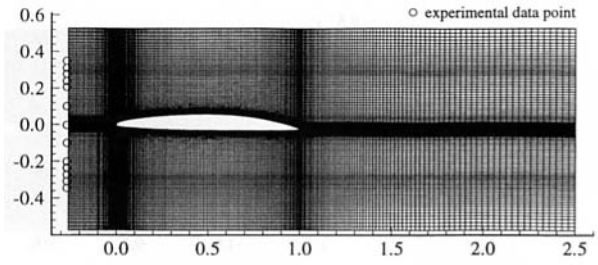

Fig. 3 Tunnel-domain grid with data locations

(1, 7, 8), verification (2–6), and validation (9, 10), and provided implementation recommendations.

Documentation of the unsteady algorithm is provided in Paterson (1994). In addition, the core CFD method has been applied to many steady-flow applications and is well documented (e.g., Stern et al., 1996).

Verification analysis consists of evaluating iterative and grid convergence, minimization of phase (i.e., time-step convergence) and dissipation errors, and determination of order-of-accuracy. Iterative convergence typically required 25 and 50 iterations for the implicit momentum and pressure/velocity-correction steps, respectively. Residuals less than 0.0001 and/or a drop of three orders of magnitude were used as the stopping criterion.

Grid convergence was studied for both steady and unsteady flow. For steady flow, the number of points in the boundary-layer and near-wall grid spacing were increased and decreased, respectively, until the change of velocity profiles and wall-shear stress between grids was approximately 1 percent. For unsteady flow, effect of axial resolution and, therefore, inherent artificial dissipation upon the wave amplitude was studied in the tunnel domain without the foil. Approximately 40 points/wavelength were required to maintain 90 percent of the amplitude at the exit of the domain. The number of points across the flapper wakes for both tunnel and complete domains was not studied.

Time-step convergence and phase error was assessed by varying the time step and comparing solution and data Fourier-series phase angles. For both small and tunnel domains, the difference in phase response, in both inviscid and viscous regions, between 50 and 64 time steps/period was approximately 0.5 percent.

Due to solution dependent FA coefficients, the order of the method is a function of cell Re and aspect ratio and, as such, the discretization does not lend itself to the typical term-by-term order-of-accuracy analysis that is common to finite-difference methods. However, using a grid-doubling scheme and Richardson extrapolation, order-or-accuracy of the core viscous-flow solver has been calculated for a variety of problems. For simple (i.e., laminar flat-plate boundary-layer and fully-developed annular-pipe flows) and complex (i.e., high Re flat plate, axisymmetric bodies, surface-piercing foils) flows (Dolphin, 1996; Zhang and Stern, 1996) with high Re (i.e., up to 10^9) and very highly stretched grids (i.e., aspect ratio up to 10^6), order-of-accuracy has been shown to range from 1.5 to 2.5. Note that this level of order-or-accuracy is comparable to, and in some cases better than, second-order finite-difference discretizations on stretched, non-orthogonal grids.

Validation, which is the purpose of this paper, is provided through detailed comparison with the MIT FFX data and is presented in the following sections.

Computational Grids and Conditions

The grids used are shown in Figs. 2–4. The small- and tunnel-domain grids have 181×80 and 180×179 points, respectively. In comparison, the complete domain has 240×179 and 71×40 points for the foil and flappers, respectively, for a total of 48,640. For each domain, approximately 40 points span the

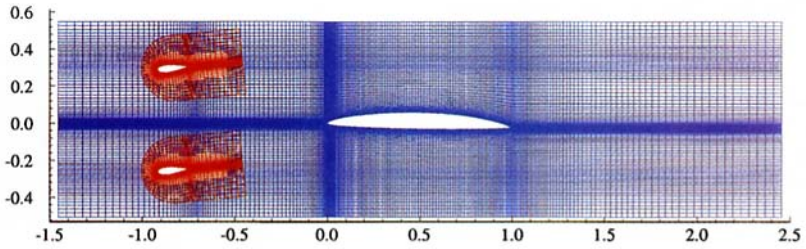

Fig. 4 Complete-domain overset-grid system

boundary-layer and the near-wall grid spacing was set such that the first grid point was located at $y^+ \approx 0.1$.

The calculations were performed at the experimental values of Re and ξ and at an angle of attack of 1.34 deg. The small-domain solution submitted for the workshop used the data for boundary conditions as previously described. Since the data did not correspond to the boundary-point locations, the data was smoothed using a cubic spline and interpolated both in time and space using a biquadratic polynomial. However, the coarseness of the data lead to erroneous results, especially for pressure. To validate the boundary condition formulation, a revised calculation was made with high resolution boundary data interpolated from the tunnel-domain solution. For tunnel-domain inlet boundary S_{td2}, smoothed and interpolated data provided approximately 60 percent of the tunnel inflow area and, as previously mentioned, the remaining 40 percent was specified by matching a potential-flow approximation to the data [see Paterson (1994) for details]. Figure 5 shows the tunnel-domain and data inlet profiles in terms of zeroth- and first-order harmonics. Also shown are second-harmonic amplitudes (U_2, V_2), which are large, particularly near the flapper wakes, and which were attributed to an excited mode of tunnel vibration (Horwich-Lurie, 1993). For the complete domain, the boundary-conditions were well-posed and required no special treatment. However, use of the Baldwin-Lomax turbulence model with overset grids presented difficulties. Because of these difficulties and the low flapper $\mathrm{Re}_L = 6.3 \times 10^5$, it was assumed that the flapper flow was laminar. Lastly, transition was fixed by forcing the eddy viscosity upstream of the boundary-layer trip to zero.

The steady-flow solution was used as the starting point for each calculation and typically 2 periods for the small domain and 4 periods for the tunnel and complete domains were required to attain a periodic solution. For the small and tunnel domains, the time step was $\frac{1}{50}$ of a period ($\Delta t = 0.01745$) and for the complete domain, the time step was $\frac{1}{64}$ of the period ($\Delta t = 0.01364$). CPU time per period and memory required on a CRAY YMP was 15 minutes/4MW, 45 minutes/6MW, and 120 minutes/8MW for the small, tunnel, and complete domains, respectively.

Discussion of Results and Comparison to Data

In the following, a brief description of the similarities and differences between the solutions on the different domains is provided. Then, using only the tunnel-domain solution, the results are compared to data and discussed in terms of the zeroth (steady) and first- and second-order (unsteady) Fourier harmonic amplitudes and phases which are defined as

$$\phi(t) = \phi_0 + \sum_{n=1}^{2} \phi_n \sin(n\xi t + \gamma_{\phi,n})$$

$$\phi_n = \sqrt{a_n^2 + b_n^2}$$

$$\gamma_{\phi,n} = \tan^{-1}(a_n/b_n)$$

$$a_n = \frac{2}{T}\int_{\tau=0}^{T} \phi(\tau)\cos(n\xi\tau)d\tau$$

$$b_n = \frac{2}{T}\int_{\tau=0}^{T} \phi(\tau)\sin(n\xi\tau)d\tau \qquad (1)$$

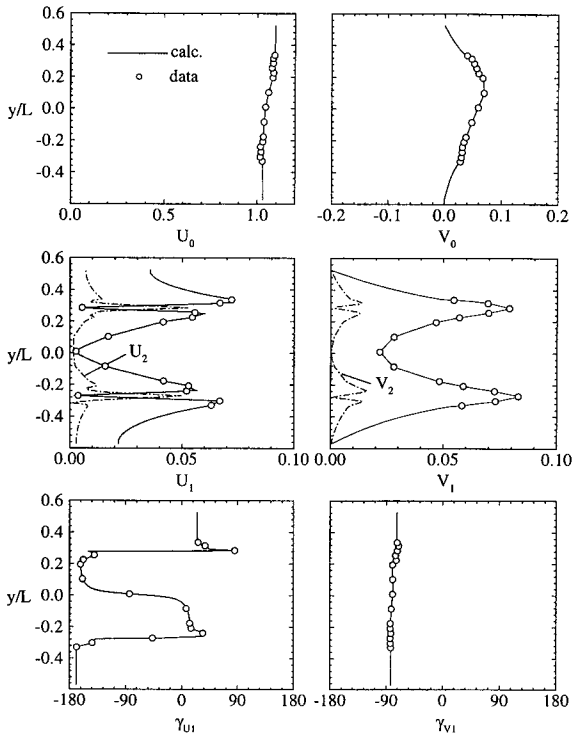

Fig. 5 Comparison of boundary data and tunnel-domain inlet conditions

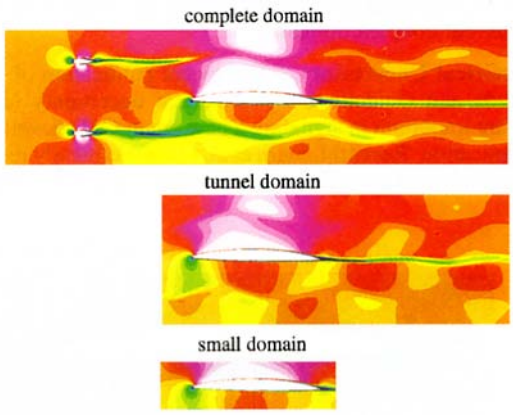

Fig. 6 Domain comparison: axial-velocity contours at $t/T = 0$

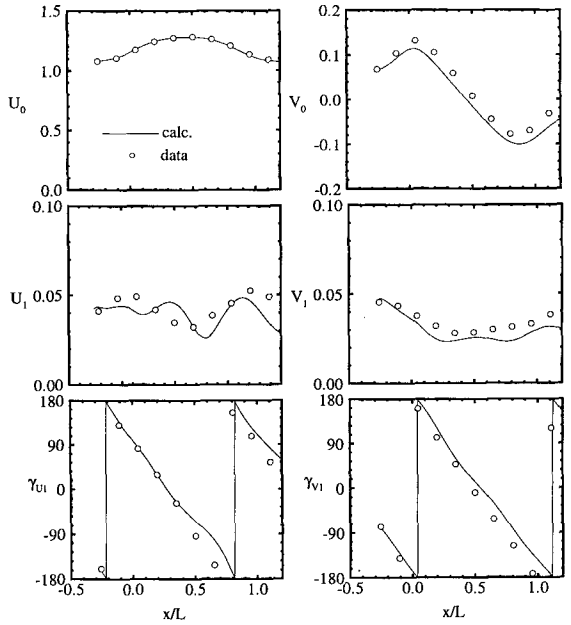

Fig. 7(*a*)

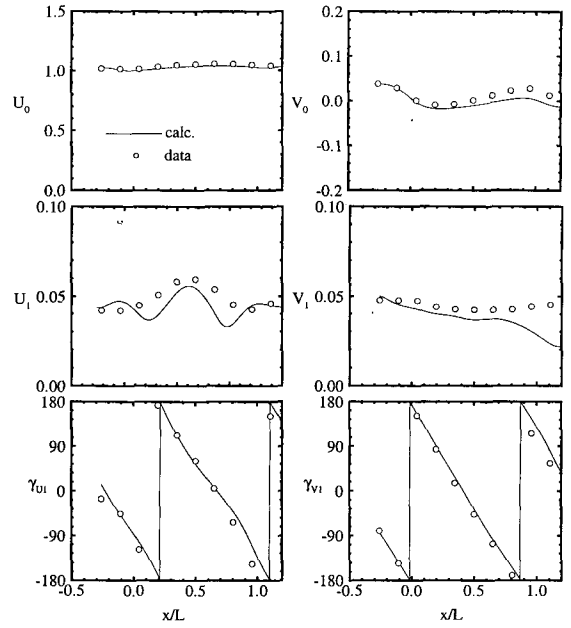

Fig. 7(*b*)

Fig. 7 Comparison of data and calculation on small-domain boundaries. (*a*) Small-domain top boundary; (*b*) small-domain bottom boundary

where ϕ represents one of the flow variables. Note that Eq. (1) was evaluated for every point in the domain by using the last period of simulation.

Comparison of Solution Domains. In Paterson and Stern (1993), it was shown that the solutions gave similar overall agreement with the data, except for the small domain with data-prescribed boundary conditions, for both steady and unsteady flow. This demonstrated that, despite differences in boundary conditions, grid generation, and CPU-time and memory requirements, complex problems could be handled with a variety of formulations. There were, however, some differences. It was shown, as previously mentioned, that the small domain with data-prescribed boundary conditions introduced erroneous higher harmonics which were attributed to the coarseness of the data. The small-domain formulation, however, was validated

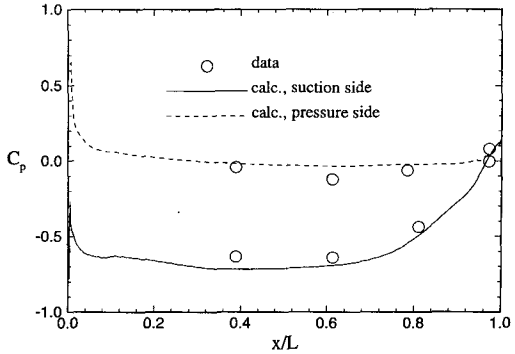

Fig. 8 Surface-pressure distribution: zeroth harmonic

by using boundary conditions prescribed by interpolating from the tunnel-domain solution. This showed nearly identical results as the tunnel domain. The inclusion of pressure-gradient effects in the turbulence model for one tunnel-domain calculation significantly improved the solution. The complete-domain solution was similar to the others, but had some small differences due to the laminar-flow treatment of the flappers, the lack of tunnel-induced vibration (i.e., response was almost purely first harmonic), and the definition of the non-dimensional velocity.

As an overall comparison, Fig. 6 shows axial-velocity contours for each of the domains at $t/T = 0$. The difference in the domain size, consistency between the solutions, and wavy nature of the flow are evident. The small- and tunnel-domain solutions are nearly identical. The complete domain shows continuity across the overlaid-grid region and flapper wakes, due to their laminar treatment, that are wider than tunnel domain and data.

Given the above discussion, the tunnel-domain solution with pressure gradient modifications will be used for discussion of the results and analysis of the response.

Steady Flow (Zeroth Harmonic). The zeroth harmonic is the same as a steady-flow solution and displays typical foil flow. Figure 7, which is a comparison in the inviscid region of the flow field on the small-domain boundaries, shows (U_0, V_0) on S_{sd1} top and bottom. U_0 and data agree and show acceleration on the suction side, whereas V_0 is similar in shape, but shows a small underprediction in comparison to the data. Surface pressure and wall-shear stress is shown in Figs 8 and 9, respectively. The pressure shows agreement with the data and the stress displays the fixed transition along with a small region of separation over the last 5 percent on the suction side. Velocity profiles, at selected stations, are shown in the left column of Fig. 10 and show good agreement with the data. This level of agreement, which required pressure-gradient modifications to the turbu-

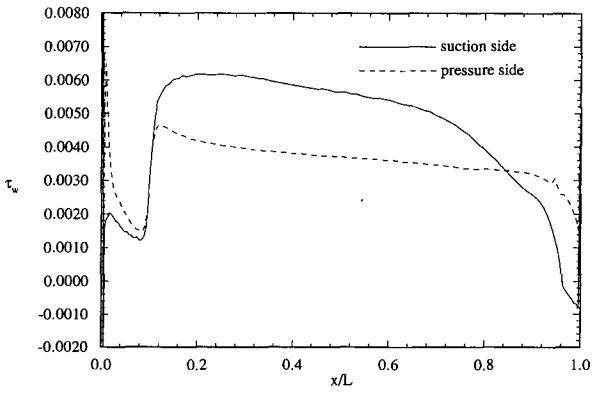

Fig. 9 Wall-shear stress distribution: zeroth harmonic

lence model, appears to be a general assessment of the current capabilities of isotropic turbulence models since it is consistent with the other participants in the FFX workshop and overall results found in the literature.

Unsteady Flow. Figure 7 includes first-harmonic amplitude (U_1, V_1) and phase (γ_{U1}, γ_{V1}). On S_{sd1} top, U_1 and data agree in magnitude and display spatial sinusoidal oscillations of nearly the same form and V_1 agrees in magnitude and shape with the data. On S_{sd1} bottom, U_1 shows agreement in both the magnitude and shape and V_1 shows an axial decay in comparison to the data. The phases are in agreement with the data on both top and bottom and show a downstream-traveling wave [in the Fourier analysis, the argument of the trigonometric functions ($\xi t + \gamma$) is equivalent to characteristic lines $\xi(t \pm x/c)$, which corresponds to downstream ($\gamma = -\xi x/c$) or upstream ($\gamma = +\xi x/c$) traveling waves].

Figure 11 shows the lift and drag time histories over one period. The lift shows a large second harmonic which is consistent with the inflow. The drag is also second harmonic and indicates a small phase lead in comparison to the lift. Figure 12 shows the surface-pressure first-harmonic amplitude and phase, the former of which has similar amplitude in comparison to the data. The shapes and zero values at certain x/L are different and unconfirmed by the limited data. A large second harmonic (figure not shown) is consistent with the lift and drag and inlet profiles. On both sides, the streamwise increasing phase indicates upstream-traveling waves which are unconfirmed by the data of nearly constant phase. It should be noted that the uncertainty of the pressure data was much debated at the ONR workshop and that, unfortunately, no estimate was provided.

Figure 13 shows the wall-shear stress first-harmonic amplitude and phase. There is no data for validation of the amplitudes, however, the phase indicates the influence of the pressure gradient: on the pressure side, decreasing values (i.e., downstream-traveling wave) on the forebody and upstream-traveling wave on the afterbody; and on the suction side, an upstream-traveling wave which leads the pressure by about 80 deg. This implies that the direction of the near-wall flow is opposite of the external-flow traveling wave.

The velocity first-harmonic amplitude and phase profiles indicate, for $x \leq 0.784$ (pressure side) and $x \leq .9$ (suction side), amplitudes with small overshoots and phases with increasing lags with x and smooth transition across the boundary layer. In contrast, for x greater than these values, a two-layer structure is displayed with relatively constant amplitude of different magnitude for the inner and outer flows with a zero amplitude and phase shift (180 deg/130 deg on suction/pressure sides) at the inner/outer boundary which is at approximately the boundary-layer edge. Figure 10 shows this at two selected stations on both sides of the foil. In the wake, where there is no data, the amplitude shows large overshoots and the phase initially shows a continuation of the boundary-layer response and then by $x = 1.1$, leads on both the pressure and suction sides. The unsteady boundary-layer response is also depicted in Fig. 14 which shows perturbation-velocity (i.e., difference between steady and unsteady) time-history contours which vividly exhibit the features previously described.

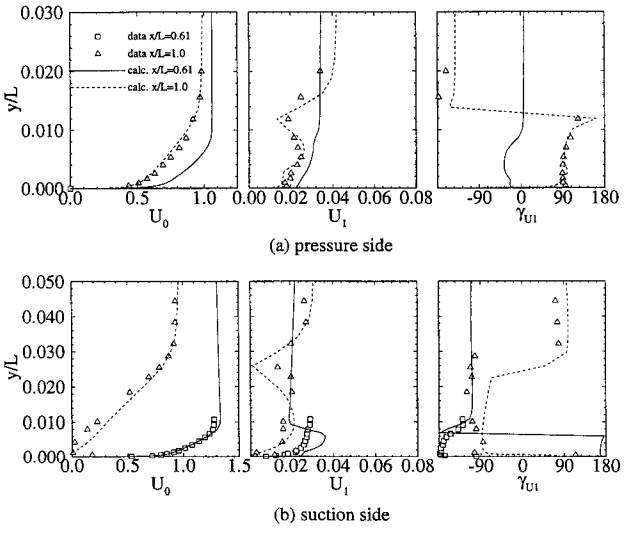

Fig. 10 Velocity profiles

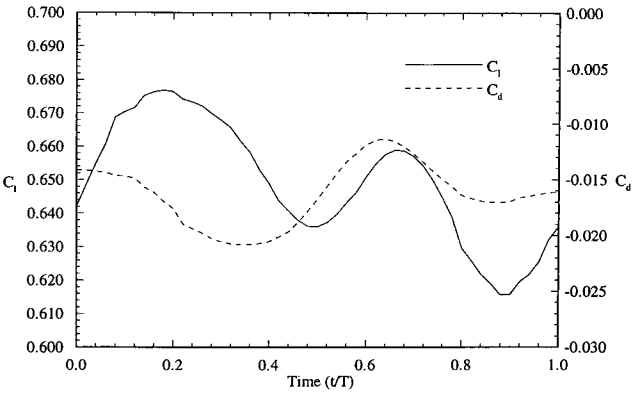

Fig. 11 Lift and drag time histories

Figure 15 shows the perturbation velocity vectors and particle traces at $t/T = 0.8$. The interaction between the flapper-wake vortices and foil is complex: distortion and increased speed on the suction (wavespeed, $c \approx 1.26$) versus the pressure ($c \approx 1.05$) side such that the flapper-wake vortices are out of phase by the time they reach the foil trailing edge; and secondary counter-rotating vortices near the trailing edge and in the wake. The latter directly correlate with and explain the region where the first-harmonic velocity profiles displayed the two-layer structure. Also, the distortion and wake complexity has similarity to that shown by Basu and Hancock (1978) and is a result of the unsteady wake sheet interacting with the distorted gust.

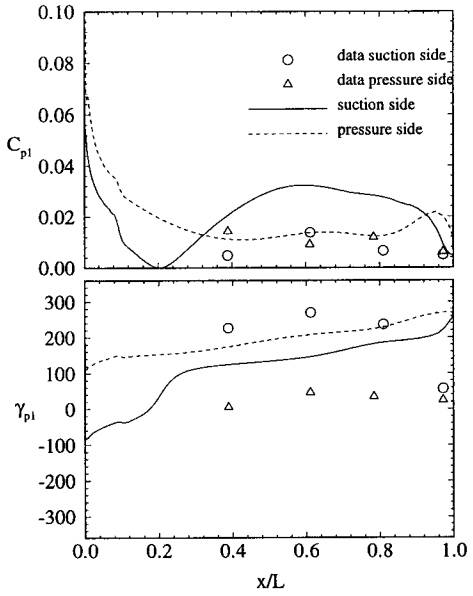

Fig. 12 Surface-pressure distribution: first harmonic amplitude and phase

Figure 15 also shows the perturbation axial pressure-gradient contours. This figure (and others in the time series which are not shown) indicates the direct correspondence between the flow pattern and axial pressure gradient, i.e., the perturbation flow directions are consistent with the regions of favorable and adverse gradients. The wake is complex, including higher harmonics and upstream- and downstream-traveling waves over the foil and in the near wake and in the intermediate wake, respectively. The upstream-traveling waves are consistent with the surface-pressure first-harmonic phase.

Analysis of Unsteady Response. To explain the unsteady response and, in particular, the nature of the correspondence between pressure gradient and external flow waves, an analysis of the pressure gradient is presented. Substituting the first three terms of the velocity Fourier series into the axial Euler equation gives

$$-\frac{\partial p}{\partial x} = p_{x_0} + \sum_{n=1}^{2} p_{x_n} \sin\left(n\xi t + \gamma_{U_n} + \hat{\gamma}_{p_{x_n}}\right) \qquad (2)$$

where p_{x_n} is the amplitude and $\hat{\gamma}_{p_{x_n}}$ is the phase shift of the pressure gradient with respect to $\gamma_{U_n} \approx -n\xi x/c$. The thirty-two terms which comprise p_{x_n} were evaluated along lines outside the boundary layer at $y^+ \approx 10^4$ (Fig. 16(a)) and it was determined that three terms, for each order, are dominant such that

$$p_{x_n} = \sqrt{\left(nU_n\xi + U_0U_n\frac{\partial\gamma_{U_n}}{\partial x}\right)^2 + \left(U_0\frac{\partial U_n}{\partial x}\right)^2}$$

$$\hat{\gamma}_{p_{x_n}} = \tan^{-1}\left(\frac{nU_n\xi + U_0U_n\dfrac{\partial\gamma_{U_n}}{\partial x}}{U_0\dfrac{\partial U_n}{\partial x}}\right) = \tan^{-1}(A) \qquad (3)$$

The first term in p_{x_n} is from the temporal derivative and the second and third, which represent steady/unsteady interaction, are from the convective term. Three cases are of particular interest:

(1) $U_n \neq U_n(x)$ (i.e., $U_{x,n} = 0$) such that $A = \pm\infty$ and $\hat{\gamma}_{p_{x_n}} = \pm\pi/2$, where + corresponds to a lead (i.e., temporal wave with $c \to \infty$) and − to a lag (i.e., spatial wave with $c \to 0$)

(2) $U_n \approx ax$ (i.e., $U_{x,n} = a$) such that A and $\hat{\gamma}_{p_{x_n}} = 0$. This corresponds to a downstream-traveling wave in phase with the velocity wave.

(3) $U_n \approx \sin(n\xi xB/c)$ (i.e., $U_{x_n} \approx \cos(n\xi xB/c)$) such that $A \approx \tan(n\xi xB/c)$ and $\hat{\gamma}_{P_{x_n}} \approx n\xi xB/c$, where

(A) $B < 1$ corresponds to a downstream-traveling wave

(B) $B = 1$ corresponds to a temporal, or stationary, wave

(C) $B > 1$ corresponds to an upstream-traveling wave.

For reference, note that a simple flat-plate boundary layer subject to a horizontal traveling waves is case (1), i.e., $U_0 = 1$, $\partial U_1/\partial x = 0$, $p_{x_1} = U_1\xi(1 - \xi/c)$, and $\hat{\gamma}_{p_{x_1}} = \pi/2$.

Figure 16(b) shows U_1 amplitudes along the evaluation lines. It is harmonic over the foil (i.e., case 3), which is consistent with the spatial oscillations shown for both EFD and CFD in Fig. 7, and linearly decreasing in the wake (i.e., case 2). Figure 16(c) is a plot of $U_1\xi + U_0U_1(\partial\gamma_{U,1}/\partial x)/U_0(\partial U_1/\partial x)$ and indicates a tangent-function behavior over the foil with $B = 1.2$ and 1.8 on the pressure and suction sides, respectively. This corresponds to upstream-traveling waves, which are consistent with Fig. 12, traveling at a wave speed of 0.2 and 0.8. In the wake, similarly strong conclusions are difficult due to departure from case 2 behavior (i.e., oscillations and singularities in A at each point where $\partial U_1/\partial x$ is zero), however, in subsequent

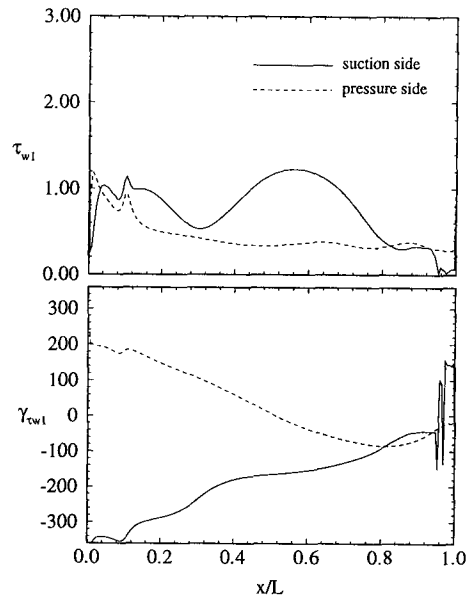

Fig. 13 Wall-shear stress distribution: first harmonic amplitude and phase

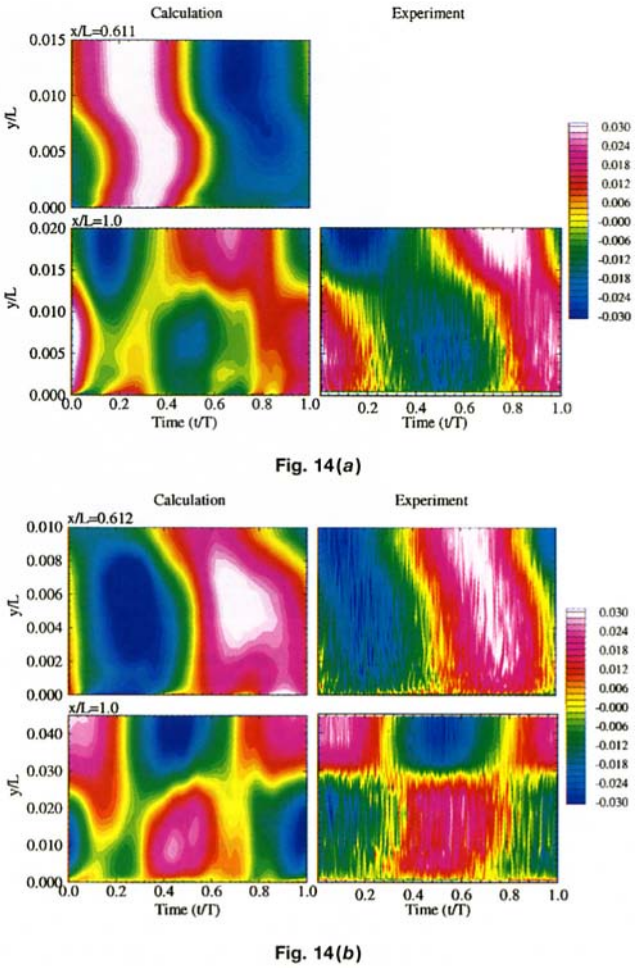

Fig. 14(a)

Fig. 14(b)

Fig. 14 Perturbation-velocity time-history contours. (a) Pressure side; (b) suction side

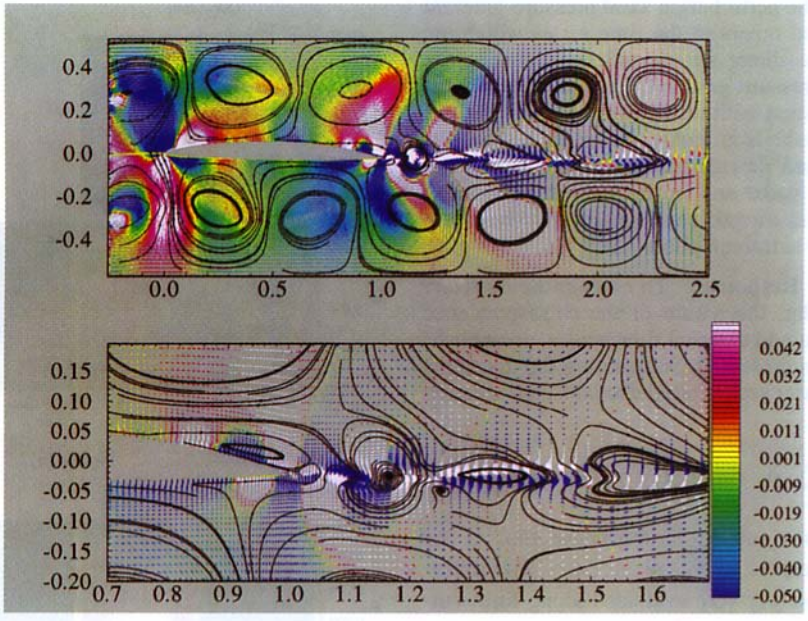

Fig. 15 Overall and detailed views of perturbation axial-pressure-gradient contours and instantaneous particle traces at $t/T = 0.8$

discussion, it is shown that the pressure-gradient exhibits downstream-traveling waves in the intermediate wake.

Figure 16(d) shows the displacement-thickness first-harmonic amplitude. Similar spatial oscillations as U_1 are observed, but with relatively larger values in the near wake. The maximum value coincides with the location where U_1 changes from oscillatory to linear behavior. This suggests viscous-inviscid interaction in the form of a pulsating near-wake displacement thickness as the source for the pressure-gradient response.

The relationship between velocity and pressure first-harmonic phases is shown in Fig. 17 for the outer ($y^+ \approx 10^4$), overlap ($y^+ \approx 200$), and sub-layer ($y^+ \approx 0.1$) regions. Also, for the outer region, the pressure-gradient phase was obtained both by differentiation of the pressure Fourier series and from the Euler-equation-derived pressure gradient Eq. (3). The pressure indicates upstream-traveling waves over the foil and a temporal, or stationary, wave in the wake downstream of the displacement-thickness peak. Also, it is nearly constant across the boundary layer. On the foil in the outer and overlap regions, the velocity shows a downstream-traveling wave, whereas in the sub-layer region it follows the pressure gradient, which is consistent with the wall-shear stress. In the wake, the velocity shows a downstream-traveling wave. The pressure gradient indicates upstream- and downstream-traveling waves over the foil and in the wake, respectively. Over the foil and in the near wake, close agreement is shown between the two pressure gradients, which validates the Euler-equation analysis.

The velocity first harmonic amplitude and phase in wall coordinates (figure not shown) shows that the largest overshoots occur near $y^+ \approx 1000$, which also corresponds to where the phase abruptly changes from the outer to inner values. The amplitudes display a double peak across the boundary layer and the phase is constant in the sublayer and the lags shown in the velocity profiles (Fig. 10) occur in the overlap region. The role of the turbulence model vs. physics for the sub-layer region is unknown, as no data is available.

Summary and Conclusions

Time-accurate RANS solutions of unsteady viscous lifting blade flows were presented and validated through comparisons with MIT FFX data. Solutions were obtained on three different domains, one of which used dynamic overset meshes, and, despite differences in boundary conditions, gave similar overall agreement. The zeroth harmonic, which was the same as steady-flow calculations, displayed typical foil response and showed that turbulence model corrections for pressure gradient were necessary for accurate solution. Despite using a quasi-steady application of the Baldwin-Lomax turbulence model, the unsteady velocity profiles showed remarkably close agreement with the data and displayed a Stokes layer response but with additional complexities such as two-layer profiles due to trailing-edge counter-rotating vortices. Unfortunately, lift and drag data were not obtained and agreement between CFD and data unsteady pressure response was poor. The CFD indicated upstream- and downstream-traveling pressure and pressure-gradient waves over the foil and in the wake, respectively. Detailed analysis showed that distortion of the external flow waves, particularly on the suction side, is significant and may be partially responsible for the complex wake structure. Also, Fourier series analysis of the velocity and axial Euler equation showed that the upstream traveling pressure waves were due to convection-induced interaction between the zeroth and first harmonics and require sinusoidal variation, as was shown by both the CFD and FFX data, of the velocity first-harmonic amplitude. The nature of the unsteady displacement thickness suggests viscous-inviscid interaction as the source of this response.

Clearly, the FFX flow is complex and requires more work to understand the variety of flow features and their implication with regard to propulsor hydrodynamics. Therefore, a parametric study is justified. In Part 2, a parametric study of frequency, waveform, and foil geometry is presented to relate the observations made in Part 1 to the classical and fundamental work on unsteady boundary layers and lifting flows, to further explicate the response observed in the FFX, and to determine implications with regard to practical applications.

Acknowledgments

This research was sponsored by ONR under Contracts N00014-92-J-1118 and N00014-91-J-1203 under the administration of Mr. Jim Fein and Dr. Ed Rood whose support is greatly appreciated. Computer funds were provided by the NASA Numerical Aerodynamic Simulation Program, the Navy

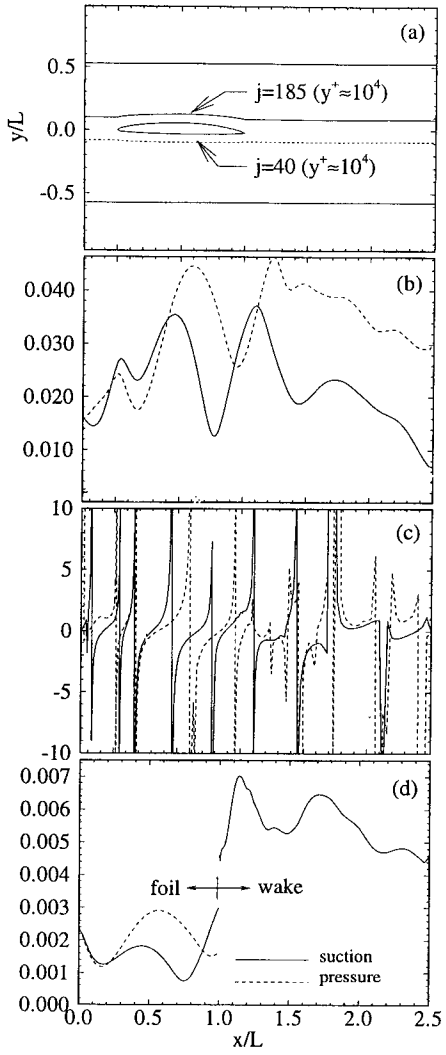

Fig. 16 Euler equation analysis. (*a*) Locations; (*b*) U_1; (*c*) $\tan(\hat{\gamma}_{p_{x_1}})$; (*d*) δ^* first-harmonic amplitude

Oceanographic Office Primary Oceanographic Prediction System, and the Army Corps of Engineers Waterways Experiment Station. The first author is grateful for the support provided by the IIHR Hunter Rouse Graduate Fellowship.

References

Attassi, H. M., Fang, J., and Patrick, S., 1993, "Direct Calculation of Sound Radiated From Bodies in Nonuniform Flows," ASME JOURNAL OF FLUIDS ENGINEERING, Vol. 115.

Basu, B. C., and Hancock, G. J., 1978, "The Unsteady Motion of a Two-Dimensional Aerofoil in Incompressible Inviscid Flow," *Journal of Fluid Mechanics,* Vol. 87.

Chen, B., Stern, F., and Kim, W. J., 1994, "Computation of Unsteady Viscous Marine Propulsor Blade and Wake Flow," *Proceedings of the 20th Symposium on Naval Hydrodynamics,* Santa Barbara, CA.

Chen, C. J., and Chen, H. C., 1984, "Finite-Analytic Numerical Method for Unsteady Two-Dimensional Navier-Stokes Equations," *Journal of Computational Physics,* Vol. 53, pp. 210–226.

Choi, J. E., Sreedhar, M., Stern, F., 1996, "Stokes Layers in Horizontal-Wave Outer Flows," ASME JOURNAL OF FLUIDS ENGINEERING, Vol. 118, No. 3.

Commerford, G. L., and Carta, F. O., 1974, "Unsteady Aerodynamic Response of a Two-Dimensional Airfoil at High Reduced Frequency," *AIAA Journal,* Vol. 12, No. 1.

Delpero, P. M., 1992, "Investigation of Flows around a Two-Dimensional Hydrofoil Subject to a High Reduced Frequency Gust Loading," M.S. thesis, Massachusetts Institute of Technology.

Dolphin, G., 1996, "Evaluation of CFD for Flat Plate, Axisymmetric, and Ship Geometries from Model to Full-Scale Reynolds Numbers," M.S. thesis, The University of Iowa.

Frietas, C. J., 1993, "Editorial," ASME JOURNAL OF FLUIDS ENGINEERING, Vol. 115, No. 3, pp. 399–400.

Goldstein, M. E., and Attasi, H. A., 1976, "A Complete Second-Order Theory for the Unsteady Flow About an Airfoil Due to a Periodic Gust," *Journal of Fluid Mechanics,* Vol. 74.

Granville, P. S., "Baldwin-Lomax Factors for Turbulent Boundary-Layers in Pressure Gradients," *AIAA Journal,* Vol. 25, No. 12, 1987, pp. 1624–1627.

Horlock, J., 1968, "Fluctuating Lift Forces on Aerofoils Moving Through Transverse and Chordwise Gusts," ASME *Journal of Basic Engineering,* pp. 494–500.

Horwich Lurie, B. 1993, "Unsteady Response of a Two-Dimensional Hydrofoil Subject to High Reduced Frequency Gust Loading," M.S. thesis, Massachusetts Institute of Technology.

Issa, R. I., 1985, "Solution of the Implicitly Discretised Fluid Flow Equations by Operator-Splitting," *Journal of Computational Physics,* Vol. 62, pp. 40–65.

Kim, H. T., and Stern, F., 1990, "Viscous Flow around a Propeller-Shaft Configuration with Infinite-Pitch Rectangular Blades," *Journal of Propulsion,* Vol. 6, No. 4, pp. 434–444.

McDonald, H., and Whitfield, D., 1996, "Self-Propelled Maneuvering Underwater Vehicles," *Proceedings of the 21st Symposium on Naval Hydrodynamics,* Trondheim, Norway.

Patel, M. H., 1975, "On Laminar Boundary Layers in Oscillatory Flow," *Proceedings of the Royal Society of London A.,* Vol. 347, pp. 99–123.

Patel, M. H., 1975, "On Turbulent Boundary Layers in Oscillatory Flow," *Proceedings of the Royal Society of London A,* Vol. 353, pp. 121–143.

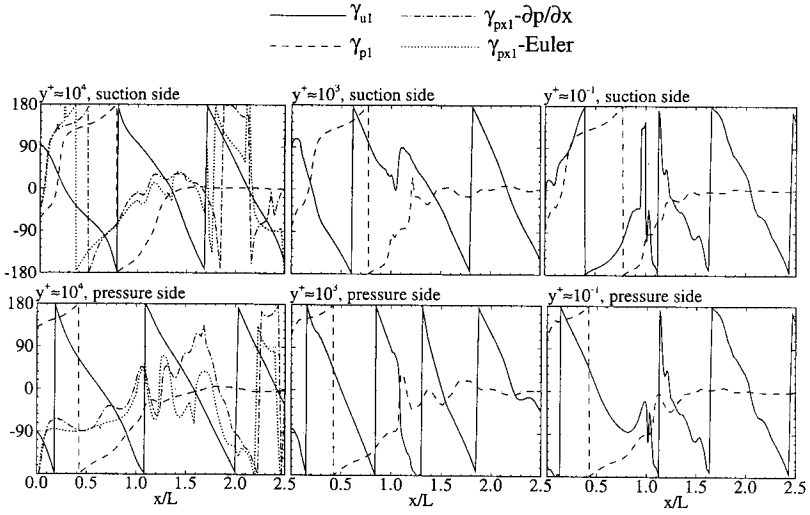

Fig. 17 Velocity, pressure, and pressure-gradient first-harmonic phase for outer, logarithmic, and sub-layer regions

Paterson, E. G., 1994, "Computation of Natural and Forced Unsteady Viscous Flow with Application to Marine Propulsors," Ph.D. thesis, The University of Iowa.

Paterson, E. G., and Stern, F., 1993, "Computation of Unsteady Viscous Flow with Application to the MIT Flapping-Foil Experiment," *Proceedings of the 6th International Conference on Numerical Ship Hydrodynamics,* Iowa City, Iowa.

Poling, D. R., and Telionis, D. P., 1986, "The Response of Airfoils to Periodic Disturbances—The Unsteady Kutta Condition," *AIAA Journal,* Vol. 24, No. 2.

Rice, J. Q., 1991, "Investigation of a Two-Dimensional Hydrofoil in Steady and Unsteady Flows," M.S. thesis, Massachusetts Institute of Technology.

Rodi, W., and Srinivas, K., 1989, "Computation of Flow and Losses in Transonic Turbine Cascades," *Z. Flugwiss. Weltraumforsch,* Vol. 13, pp. 101–119.

Sears, W. R., 1941, "Some Aspects of Non-Stationary Airfoil Theory and Its Practical Application," *Journal of Aeronautical Sciences,* Vol. 8.

Shima, N., 1993, "Prediction of Turbulent Boundary Layers with Second-Moment Closure: Part 1—Effects of Periodic Pressure Gradient, Wall Transpiration, and Free-Stream Turbulence," ASME JOURNAL OF FLUIDS ENGINEERING, Vol. 115, No. 1.

Spalart, P. R., and Baldwin, B. S., 1989, "Direct Simulation of a Turbulent Oscillating boundary Layer," *Turbulent Shear Flows 6,* J. C. Andre et al., eds., Spring-Verlag.

Stern, F., Paterson, E. G., and Tahara, Y., 1996, "CFDSHIP-IOWA: Computational Fluid Dynamics Method for Surface-Ship Boundary Layers, Wakes, and Wave Fields," IIHR Report 381, Institute of Hydraulic Research, The University of Iowa.

Stern, F., Kim, H. T., Zhang, D. H., Toda, Y., Kerwin, J., and Jessup, S., 1994a, "Computation of Viscous Flow around Propeller-Body Configurations: Series 60 C_B = .6 Ship Model," *Journal of Ship Research,* Vol. 38, No. 2, pp. 137–157.

Stern, F., Zhang, D. H., Chen, B., Kim, H. T., and S. D. Jessup, 1994b, "Computation of Viscous Flow around Propeller-Shaft Configurations," *Proceedings of the 20th Symposium on Naval Hydrodynamics,* Santa Barbara, CA.

Suhs, N. E., and Tramel, R. W., 1991, "PEGSUS 4.0 User's Manual," Arnold Engineering Development Center, AEDC-TR-91-8.

Telionis, D. P., 1981, *Unsteady Viscous Flow,* New York, Springer-Verlag.

Thompson, J. F., 1987, "A Composite Grid Generation Code for General 3-D Regions," *AIAA 25th Aerospace Sciences Meeting,* Reno, NV.

Zhang, Z., and Stern, F., 1996, "Wave-Induced Separation," ASME JOURNAL OF FLUIDS ENGINEERING, Vol. 118, No. 3.